Water and Vapor Movement with Condensation and Evaporation in a Sandy Column

Masaru Sakai*

Dep. of Environmental Sciences
Univ. of California
Riverside, CA 92521

Nobuo Toride

Graduate School of Bioresources
Mie Univ.
Tsu City
Japan 514-8507

Jiří Šimůnek

Dep. of Environmental Sciences
Univ. of California
Riverside, CA 92521

The diffusion of warm, humid air into an initially cold, dry, sandy column was analyzed to study the movement of water vapor and liquid water under nonisothermal and low water content conditions. The analysis was performed using the HYDRUS-1D code. While the water retention curve of sand was measured experimentally, the unsaturated hydraulic conductivity function was inversely estimated from the observed water content profiles in the column. The estimated unsaturated hydraulic conductivity function displayed a shape that reflected distinct processes of capillary pore water flow and film flow at high and low water contents, respectively. Four components of the total water flux, including thermal and isothermal liquid water and water vapor fluxes, were evaluated using the calibrated soil hydraulic properties. Evaporation and condensation rates were calculated based on water mass balance. Water vapor entered the soil column at the hot surface and condensed at the cold bottom. Subsequently, liquid water moved upward and evaporated at the moisture front in the middle of the column where the relative humidity decreased below unity. Liquid water and water vapor then circulated between the bottom and the moisture front, accompanied by condensation and evaporation processes. The impact of the enhancement factor in the thermal vapor diffusion term could not be clearly identified from available experimental water content profiles. Increases in liquid water flow and the evaporation rate could be compensated for by increases in vapor flow and the condensation rate. Additional data would be needed to fully evaluate the effect of the enhancement factor.

Complex processes involved in the surface energy balance produce diurnal fluctuations of the air temperature at the soil–atmosphere interface, inducing either water vapor evaporation or condensation at different times of the day. Since water vapor flow in semiarid and arid regions can represent a major part of the overall water flow, it is important to take it into account together with liquid water flow when evaluating hydrologic fluxes and solute transport (Milly, 1984; Scanlon et al., 2003). Additionally, water vapor flow significantly affects the movement of heat, since it transports a substantial amount of energy as the latent heat of vaporization (Cahill and Parlange, 1998; Saito et al., 2006). Hence, the simultaneous evaluation of liquid water, water vapor, and heat movement in soils is essential for many applications in research as well as in water management.

Penman (1940) first developed a theory of vapor flow in soils based on Fick's law. Later, Philip and de Vries (1957) mathematically extended Penman's theory to describe coupled movement of liquid water and water vapor under nonisothermal conditions. They divided the total water flux into four components, consisting of liquid water and water vapor fluxes driven by either water content or temperature gradients. Philip and de Vries (1957) also introduced an enhancement factor for vapor flux due to the temperature gradient. Water vapor could move through a "liquid island" in a soil pore, condensing at one end and evaporating at the other. Another reason for the enhanced vapor movement is that the actual local temperature gradient in air-filled pores may be significantly greater than the average temperature gradient for the bulk soil. Since the enhancement factor is difficult to measure directly, Cass et al. (1984) estimated this parameter indirectly based on the pressure head dependence of the thermal conductivity. Nassar and Horton (1989) and Nassar et al. (1992b) further extended the Philip and de Vries (1957) model by including osmotic effects on liquid water and water vapor movement.

It is essential to precisely determine soil hydraulic properties at low water saturations when describing liquid water flow in dry soils. Although many methods exist to determine soil hydraulic properties (Klute and Dirksen, 1986), unsaturated hydraulic conductivity at low water saturations is very difficult to measure. Only methods based on flow under accelerated gravitational (centrifugal) conditions seem to be practical for low water saturations (e.g., Nimmo, 1990). In recent years, several inverse methods, such as the multistep outflow method (Eching and Hopmans, 1993; Inoue et al., 1998) and the evaporation method (Šimůnek et al., 1998; Fujimaki and Inoue, 2003) have been developed to estimate unsaturated hydraulic properties from experimentally obtained data involving transient water flow. Although these methods usually cover only a relatively high water content range (i.e., above the measurement range of a tensiometer), it should be possible to extend the application of these methods to drier soils, providing that a

soil hydraulic property model correctly describes retention and conductivity properties in the dry water content range.

One of the most widely used functions for describing unsaturated hydraulic properties is van Genuchten's (1980) set of closed-form equations for the soil water retention curve, coupled with Mualem's (1976) pore-size distribution model for the unsaturated hydraulic conductivity function. The van Genuchten (1980) model sometimes fails to describe soil water retention properties, however, and underestimates the unsaturated hydraulic conductivity at low water contents. Tuller and Or (2001) showed a relation between the unsaturated hydraulic conductivity and the pressure head based not only on the pore-size distribution, but also film flow on the surface of soil particles, a process that dominated at low saturations. Fayer and Simmons (1995) modified the van Genuchten soil water retention model to better describe soil water retention at low water contents and described the unsaturated hydraulic conductivity function by coupling their model with the Mualem (1976) model. The Mualem model contains the pore-connectivity coefficient that accounts for the effects of pore connectivity and tortuosity, which can have a significant impact on the gradient of the unsaturated hydraulic conductivity with respect to the pressure head. Although Mualem (1976), based on an analysis of 45 soil samples, suggested the average value of the pore-connectivity coefficient to be 0.5, some recent studies had utilized other values (e.g., Romano and Santini, 1999; Hopmans et al., 2002; Schaap et al., 2001).

Although numerical simulations of the simultaneous movement of liquid water, water vapor, and heat in soils with medium or high water contents have been performed in the past (e.g., Nassar et al., 1992b), few simulations have been performed for relatively dry soils. This is largely because of uncertainty about unsaturated hydraulic conductivity. The objective of this study was to evaluate the vapor condensation experiments performed by Miyazaki (1976) using the Philip and de Vries (1957) theory and the Fayer and Simmons (1995) hydraulic property model implemented in the HYDRUS-1D code (Šimůnek et al., 2008a,b; Saito et al., 2006). These laboratory experiments involved coupled movement of liquid water, water vapor, and heat in sandy columns under an imposed temperature gradient. During the experiments, water vapor diffused from the hot and humid end of the columns and subsequently condensed at the cold dry end. In our study, the water retention curve parameters were first fitted to independently measured water retention curve data using the Fayer and Simmons (1995) model. The numerical model was then calibrated against experimental data of volumetric water content profiles by inversely estimating the pore-connectivity coefficient to determine the unsaturated hydraulic conductivity function for low water contents while using independently fitted water retention curve parameters. Further analyses of various processes were then performed using the calibrated model. Second, four components of the total water flux, including liquid and vapor fluxes due to pressure head and temperature gradients, were evaluated using calculated pressure head and temperature profiles. Third, condensation and evaporation rates were calculated from the mass balance and liquid water and water vapor fluxes. Fourth, the impact of the enhancement factor on the coupled transport involving condensation and

evaporation processes was investigated. Finally, the uncertainty of the inverse parameter estimation procedure using the available data set was determined and the need for additional data to guarantee a unique solution was recognized.

MATERIALS AND METHODS
Condensation Experiments

Miyazaki (1976) conducted one-dimensional laboratory column experiments to observe the diffusion of water vapor from hot and humid air into cold and dry soil and to evaluate the various mechanisms involved in water vapor flow. The experiments were performed using Hamaoka dune sand, which had the typical particle size distribution of dune sand. It contained 3% of soil particles in the range of 0.002 to 0.02 mm, 7% of soil particles in the range of 0.02 to 0.1 mm, and 90% of soil particles >0.1 mm. The saturated hydraulic conductivity of 34.6 m d^{-1} was measured using the falling-head method. Hamaoka dune sand with an initial volumetric water content of 0.0045 m^3 m^{-3} was packed uniformly at a dry bulk density of 1.6 g cm^{-3} in six acrylic columns with 10-cm height and 10-cm diameter. The sand columns were then placed vertically in a chamber with a constant air temperature of 37°C and relative humidity of 85 to 90%. The tops of the columns were exposed to the moist air, while the closed bottoms of the columns were maintained at 20°C by circulating constant-temperature water along the base of the columns using a water pump. The walls of the columns were insulated using foam polystyrene to achieve one-dimensional heat flow. Since differences between the observed temperatures at the center and close to the wall of the column were <0.6°C (or 12°C m^{-1}), the experiment was assumed to have one-dimensional heat flow.

Because of the difference in the vapor density between the two ends of the columns, water vapor diffused from the hot and humid end of the column toward the cold and dry end, where it condensed. Subsequently, the condensed liquid water moved upward due to the pressure head gradients. Temperature profiles in the columns were monitored with thermocouples located at depths of 0, 2, 5, 8, and 10 cm at the center of the columns. The amount of cumulative water vapor diffusion into the column was measured based on the column weights. Identical experiments were repeated on all six columns to obtain water content profiles at different times (2, 5, 10, 16, 21, and 30 d). Each sand column at those times was sectioned into seven 1- and 2-cm-thick layers to gravimetrically determine the water contents.

Numerical Model
Unsaturated Water Flow

Darcy's law for liquid water flux, q_L, under time-variable temperature conditions has to consider both the flow driven by the temperature gradient, accounting for the temperature dependence of the surface tension, as well as the term driven by the pressure head gradient (Philip and de Vries, 1957). Since the vapor density is also a function of the pressure head and the temperature, Fick's law for the vapor flux, q_v, also consists of two (thermal and isothermal) components. Thus, the total water flux, q_{Total}, in a variably saturated soil is the sum of the liquid water flux and the water vapor flux:

$$q_{Total} = q_L + q_v = q_{Lh} + q_{LT} + q_{vh} + q_{vT}$$

$$= -K_{Lh}\left(\frac{\partial h}{\partial z} + 1\right) - K_{LT}\frac{\partial T}{\partial z} - K_{vh}\frac{\partial h}{\partial z} - K_{vT}\frac{\partial T}{\partial z} \quad [1]$$

where q_{Lh} and q_{LT} are the isothermal and thermal liquid water fluxes [L T^{-1}], respectively; q_{vh} and q_{vT} are the isothermal and thermal water vapor fluxes [L T^{-1}], respectively; h is the pressure head [L]; T is the temperature [K]; z is the spatial coordinate positive upward [L]; K_{Lh} [L T^{-1}] and K_{LT} [L^2 K^{-1} T^{-1}] are the isothermal and thermal hydraulic conductivities for liquid water fluxes, respectively; and K_{vh} [L T^{-1}] and K_{vT} [L^2 K^{-1} T^{-1}] are the isothermal and thermal vapor hydraulic conductivities, respectively. Inserting Eq. [1] into the mass conservation equation leads to the Richards equation for nonisothermal conditions (e.g., Nassar and Horton, 1997; Noborio et al., 1996):

$$\frac{\partial \theta}{\partial t} = -\frac{\partial q_{Total}}{\partial z}$$
$$= \frac{\partial}{\partial z}\left[K_{Lh}\left(\frac{\partial h}{\partial z}+1\right) + K_{LT}\frac{\partial T}{\partial z} + K_{vh}\frac{\partial h}{\partial z} + K_{vT}\frac{\partial T}{\partial z}\right] \quad [2]$$

where θ is the total volumetric water content [L^3 L^{-3}] and t is time [T].

This mass conservation equation can be divided into two equations that account for liquid water and water vapor contents (Nassar and Horton, 1992):

$$\frac{\partial \theta_L}{\partial t} = -\frac{\partial q_L}{\partial z} - E \quad [3]$$

$$\frac{\partial \theta_v}{\partial t} = -\frac{\partial q_v}{\partial z} + E \quad [4]$$

where θ_L is the volumetric liquid water content [L^3 L^{-3}], θ_v is the volumetric vapor content expressed as an equivalent amount of liquid water per unit volume of the soil [L^3 L^{-3}], and E is the evaporation or condensation rate [T^{-1}] (positive for evaporation and negative for condensation).

Soil Hydraulic Properties

A model proposed by Fayer and Simmons (1995) (denoted below as the Fayer model) was used for the soil water retention curve. They modified the residual water content in the van Genuchten model (van Genuchten, 1980) to better represent the soil water retention curve at low water contents. The model accounts for the adsorption of water on soil under dry conditions:

$$\theta_L = \chi \theta_a + (\theta_s - \chi \theta_a)\left[1 + (-\alpha h)^n\right]^{-m} \quad [5]$$

where θ_s is the saturated water content [L^3 L^{-3}], and α [L^{-1}], n (dimensionless), m ($= 1 - 1/n$), and θ_a [L^3 L^{-3}] are empirical shape parameters. The first term, $\chi \theta_a$, denotes adsorption of water on soil and χ is described as

$$\chi(h) = 1 - \frac{\ln(-h)}{\ln(-h_m)} \quad [6]$$

where h_m is the pressure head at the water content equal to 0, and is generally taken to be -10^7 cm (Rossi and Nimmo, 1994).

The closed form of the isothermal hydraulic conductivity function for the liquid water flux, K_{Lh}, is obtained for the Fayer model by substituting Eq. [5] into the pore-size distribution model of Mualem (1976):

$$K_{Lh} = K_s S_e^{\ l}\left[\frac{\int_0^{S_e} dS_e/|h|}{\int_0^1 dS_e/|h|}\right]^2 = K_s S_e^l\left[\frac{\Gamma_s(h)}{\Gamma_{max}}\right]^2 \quad [7]$$

where K_s is the saturated hydraulic conductivity [L T^{-1}], S_e ($= \theta_L/\theta_s$) is the effective liquid saturation (dimensionless), and l is the pore-connectivity coefficient that was assumed to be 0.5 in the original study. The definitions of $\Gamma_s(h)$ and Γ_{max} are presented in Fayer and Simmons (1995).

The thermal hydraulic conductivity for the liquid water flux, K_{LT}, is defined as (e.g., Noborio et al., 1996)

$$K_{LT} = K_{Lh}\left(hG_{wT}\frac{1}{\gamma_0}\frac{d\gamma}{dT}\right) \quad [8]$$

where γ is the surface tension of soil water [M T^{-2}] and γ_0 is the surface tension at 25°C (= 71.89 g s^{-2}). The gain factor, G_{wT}, which corrects the temperature dependence of the surface tension, was fixed at 7 in this study (Nimmo and Miller, 1986).

Hydraulic conductivities for vapor phase fluxes due to pressure head, K_{vh}, and temperature, K_{vT}, gradients are defined as

$$K_{vh} = \frac{D}{\rho_w}\rho_{vs}\frac{Mg}{RT_{abs}}H_r \quad [9]$$

$$K_{vT} = \frac{D}{\rho_w}\eta H_r\frac{d\rho_{vs}}{dT} \quad [10]$$

respectively, where D is the vapor diffusivity in soil [L^2 T^{-1}], ρ_w is the density of liquid water [M L^{-3}], ρ_{vs} is the saturated vapor density [M L^{-3}], M is the molecular weight of water [M mol^{-1}] (= 0.018015 kg mol^{-1}), g is the gravitational acceleration [L T^{-2}] (= 9.81 m s^{-2}), R is the universal gas content [M L^2 T^{-2} mol^{-1} K^{-1}] (= 8.341 J mol^{-1} K^{-1}), T_{abs} is the absolute temperature [K], H_r is the relative humidity, and η is the enhancement factor. A formulation derived by Cass et al. (1984) and Campbell (1985) was used for η:

$$\eta = a + 3\frac{\theta_L}{\theta_s} - (a-1)\exp\left\{-\left[\left(1+\frac{2.6}{\sqrt{f_c}}\right)\frac{\theta_L}{\theta_s}\right]^3\right\} \quad [11]$$

where f_c is the mass fraction of clay in the soil (dimensionless) (fixed at 0.02 in this study) and a is a constant. As discussed below in relation to Fig. 11, we assumed that $a = 8$ for the Hamaoka dune sand, based on the study of Cass et al. (1984) on lysimeter sand. The vapor diffusivity in soil can be derived from the diffusivity of water vapor in air, D_a [L^2 T^{-1}], multiplied by the tortuosity factor in the gaseous phase, τ_a (Millington and Quirk, 1961), and the volumetric air content, θ_{air} [L^3 L^{-3}]:

$$D = \tau_a \theta_{air} D_a = \frac{\theta_{air}^{7/3}}{\theta_s^2}\theta_{air} D_a \quad [12]$$

Selected parameters used in the numerical simulations are shown in Table 1.

Heat Transport

The principle of heat conservation is described as (de Vries, 1958)

$$\frac{\partial C_p T}{\partial t} + L_0\frac{\partial \theta_v}{\partial t} = \frac{\partial}{\partial z}\left[\lambda(\theta_L)\frac{\partial T}{\partial z}\right] - C_w\frac{\partial q_L T}{\partial z} - C_a\frac{\partial q_v T}{\partial z} - L_0\frac{\partial q_v}{\partial z} \quad [13]$$

where L_0 ($= L_w\rho_w$) is the volumetric latent heat of vaporization of water (J m^{-3}), L_w (= 2.501 × 10^6 − 2369.2T) is the latent heat of vaporization of water (J kg^{-1}), and $\lambda(\theta_L)$ is the soil thermal conductivity [M L T^{-3} K^{-1}] described as (Chung and Horton, 1987)

Table 1. Parameters used in numerical simulations.

Parameter	Equation†	Reference
Surface tension of soil water (γ), g s^{-2}	$\gamma = 75.6 - 0.1425T - 2.38 \times 10^{-4}T^2$	Hillel (1971)
Density of liquid water (ρ_w), kg m^{-3}	$\rho_w = 1 - 7.37 \times 10^{-6}(T-4)^2 + 3.79 \times 10^{-8}(T-4)^3$	Hillel (1971)
Saturated vapor density (ρ_{vs}), kg m^{-3}	$\rho_{vs} = \exp(31.37 - 6014.79T_{abs}^{-1} - 7.92 \times 10^{-3}T_{abs})T_{abs}^{-1} \times 10^{-3}$	Campbell (1985)
Diffusivity of vapor in air (D_a), m^2 s^{-1}	$D_a = 2.12 \times 10^{-5}(T_{abs}/273.15)^2$	Campbell (1985)
Relative humidity (H_r)	$H_r = \exp(hMg/RT_{abs})$	Philip and de Vries (1957)
Latent heat of vaporization of water (L_w), J kg^{-1}	$L_w = 2.501 \times 10^6 - 2369.2T$	Monteith and Unworth (1990)

† T, temperature; T_{abs}, absolute temperature; h, pressure head; M, molecular weight of water; g, gravitational acceleration; R, universal gas constant.

$$\lambda(\theta_L) = b_1 + b_2\theta_L + b_3\theta_L^{0.5} \quad [14]$$

where b_1, b_2, and b_3 are constants (for sands, $b_1 = 0.228$ W m^{-1} K^{-1}, $b_2 = -2.406$ W m^{-1} K^{-1}, and $b_3 = 4.909$ W m^{-1} K^{-1}, as implemented in the HYDRUS-1D code). The two terms on the left-hand side of Eq. [13] represent changes in the energy content and the latent heat of the vapor phase. The terms on the right-hand side of Eq. [13] represent soil heat flow by conduction, the convection of sensible heat with flowing water, the transfer of sensible heat by diffusion of vapor, and the transfer of latent heat by diffusion of vapor. The volumetric heat capacity of the soil, C_p [M L^{-1} T^{-2} K^{-1}] is defined as the sum of the volumetric heat capacities of the solid C_n (= 1.92 MJ m^{-3} K^{-1}), liquid C_w (= 4.18 MJ m^{-3} K^{-1}), and air C_a (= 6.3 kJ m^{-3} K^{-1}) phases multiplied by their respective volumetric fractions θ (de Vries, 1958):

$$C_p = C_n\theta_n + C_w\theta_L + C_a\theta_a \quad [15]$$

where θ_n is the volumetric fraction of the solid phase [L^3 L^{-3}]. The third term is usually neglected because it is significantly smaller than the other two terms.

Initial and Boundary Conditions

Initial and boundary conditions were based on the condensation experiment. The initial volumetric water content was assumed to be uniform throughout the soil column (i.e., $\theta_L = 0.0045$). The corresponding initial pressure head, calculated from the water retention curve (Eq. [5]), was approximately -7×10^5 cm. The upper boundary condition for water flow was given by the total incoming water flux:

$$q_{Total}(0,t) = (q_{Lh} + q_{LT} + q_{vh} + q_{vT})\big|_{z=0} \quad (t > 0) \quad [16]$$

The total surface flux, $q_{Total}(0,t)$, was assumed to be equal to the change in weight of the entire column, thus reflecting the condensation of water vapor in the column. We fitted a quadratic curve to the observed increase in weight of the column (cumulative condensation), and determined $q_{Total}(0,t)$ from the time derivative of this curve.

It was assumed that there was no water flux at the lower boundary describing the closed end of the column:

$$q_{Total}(-10,t) = (q_{Lh} + q_{LT} + q_{vh} + q_{vT})\big|_{z=-10} = 0 \quad (t > 0) \quad [17]$$

The sum of the liquid water flux (the sum of q_{Lh} and q_{LT}) and the vapor flux (the sum of q_{vh} and q_{vT}) must be zero to satisfy the no-flux boundary condition.

Since only measured temperature profiles for the 6th and 16th days were available from Miyazaki (1976), the initial temperature was assumed to be a constant room temperature of 23.5°C throughout the soil profile. Dirichlet boundary conditions with specified temperatures were considered for heat transport calculations. As it is unlikely that the boundary temperatures of the soil are equal to imposed temperatures (Farlow, 1993, p. 19–26), the upper and lower boundary temperatures were set equal to the average temperatures observed at those locations nearest to both boundaries, i.e., 36.3°C at the soil surface and 23.5°C at the soil bottom.

Governing Eq. [2] and [13] describing coupled movement of liquid water, heat, and water vapor were solved numerically using the HYDRUS-1D code that included vapor transport (Šimůnek et al., 2008a,b). The soil column was discretized uniformly into finite elements of 0.1 cm. The time step was allowed to vary between the initial and maximum allowed time steps of 1×10^{-10} and 0.01 d, respectively.

Hydraulic Parameters

Figure 1a shows water retention curves for the Hamaoka dune sand measured using both drainage and imbibition processes. Since Miyazaki (1976) did not provide the water retention curve, both processes were observed using a hanging water column. A time domain reflectometry (TDR) probe (three 6.5-cm-long metallic rods of 0.15-cm diameter with 0.5-cm separations) and a tensiometer (having a 1.5-cm-long and 0.6-cm-diameter porous cup) with a pressure transducer were installed horizontally in a soil sample with a height of 2 cm and an internal diameter of 10 cm. After draining from saturation to a pressure head of –60 cm, the imbibition pro-
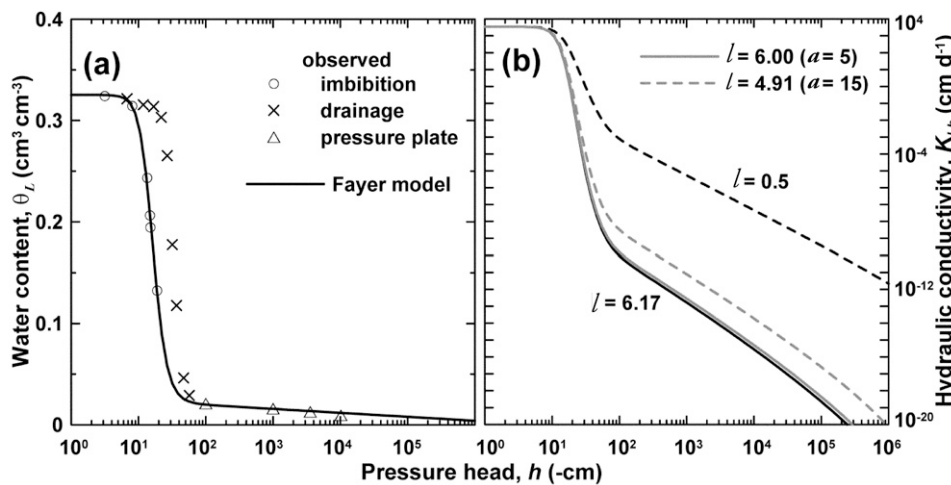

Fig. 1. (a) The soil water retention curve of the Hamaoka dune sand, with the Fayer and Simmons (1995) model fitted to the imbibition data; and (b) unsaturated hydraulic conductivity functions evaluated using pore-connectivity coefficient (l) values of 0.5, 4.91, 6.00, and 6.17.

cess was subsequently performed by connecting the soil sample with a Mariotte tank and returning it to saturation. Finally, the drainage curve was measured and the final water content at –60 cm was determined gravimetrically. The TDR measurements were then calibrated based on the final water content and the cumulative amount of drainage. Using this calibration, dielectric constants measured during the imbibition process were then converted to volumetric water contents. We used the water content values estimated by TDR in Fig. 1a. The water retention curve for soils with lower water contents was then measured using the pressure-plate apparatus for pressure heads lower than –100 cm (see Fig. 1a) and assuming that hysteresis could be ignored for these low pressure heads.

Since the Hamaoka dune sand displayed a relatively important hysteretic behavior and because the condensation experiment represented a wetting process during the entire period, the imbibition water retention curve was used in the calculations. The Fayer model (Eq. [5]) was fitted to the observed data, resulting in values of θ_a = 0.027, θ_s = 0.325, α = 0.0656 cm^{-1}, and n = 4.71. Note that θ_s was about 0.06 smaller than the porosity value of 0.385 calculated from bulk and particle densities. This was probably partly due to the inevitably entrapped air during the drainage and imbibition processes. Furthermore, since we estimated θ_s based on the final water content at h = –60 cm and the cumulative drainage amount, θ_s might be slightly underestimated. Since the condensation experiment was performed in the pressure head range below –20 cm, we believe that these possible experimental errors near saturation did not affect our calculations.

Figure 1b shows the relation between the pressure head, h, and the unsaturated hydraulic conductivity, K_{Lh}, derived by substituting Fayer's water retention curve model (Eq. [5]) into Mualem's model (Eq. [7]). The observed value of the saturated hydraulic conductivity (K_s = 34.6 m d^{-1}) and the value of the pore-connectivity coefficient suggested by Mualem (l = 0.5) were used to obtain the unsaturated hydraulic conductivity function. The gradient, $\mathrm{d}\log K_{Lh}/\mathrm{d}\log h$, is larger for the higher pressure head range (–10 ≥ h ≥ –100 cm) than for the lower pressure head range (h < –100 cm).

When the a parameter in the enhancement factor is assumed to be known (i.e., equal to 8 (Eq. [11]), the pore-connectivity coefficient l is the only remaining unknown parameter (when not assumed to be 0.5). Therefore, the value of l was optimized using an inverse analysis (e.g., Šimůnek et al., 1998), during which the numerical solution was fitted to volumetric water contents observed in the vapor condensation experiment. Parameters θ_a, θ_s, α, n, and K_s were kept constant at the values discussed above during the inverse analyses. The objective function, Φ, was defined as

$$\Phi = \sum_{j=1}^{n_j} \sum_{i=1}^{n_i} \left[\theta_L^*\left(z_j, t_i\right) - \theta_L\left(z_j, t_i\right) \right]^2 \qquad [18]$$

where $\theta_L^*(z_j, t_i)$ and $\theta_L(z_j, t_i)$ were the observed and calculated water contents at time t_i for the spatial coordinate z_j, respectively, n_i was the number of measurement times, and n_j was the number of measurement locations. Minimization of the objective function, Φ, was accomplished using the Levenberg–Marquardt nonlinear minimization method (Marquardt, 1963).

The impact of the enhancement factor, η, on the optimized l parameter in the unsaturated hydraulic conductivity, K_{Lh}, was evaluated by performing the model calibration with different values of the a parameter (= 5, 8, or 15) in Eq. [11] (Fig. 2). We also demonstrated how
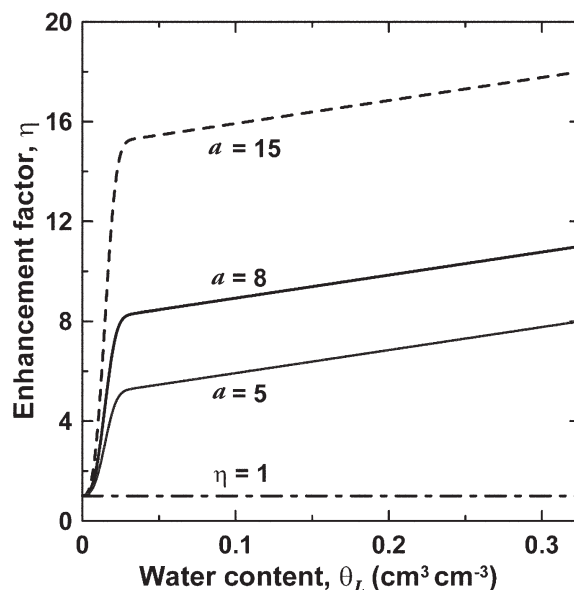

Fig. 2. Enhancement factors for different values of the a parameter (Eq. [11]).

water content profiles and water fluxes change when different values of the enhancement factor (with a = 5, 8, or 15 or η = 1) were used.

RESULTS AND DISCUSSION
Unsaturated Hydraulic Conductivity

The liquid water content profiles were first calculated with the original values of the pore-connectivity coefficient (l = 0.5) suggested by Mualem (1976) and the enhancement factor (a = 8) suggested by Cass et al. (1984). Figure 3 compares the calculated and observed water content profiles. Similar to the observed water contents, the calculated water contents also increased from the bottom due to vapor condensation; however, the shape of the simulated water content profiles was quite different from those observed. It was found that the simulated water contents were much smaller than the observed values near
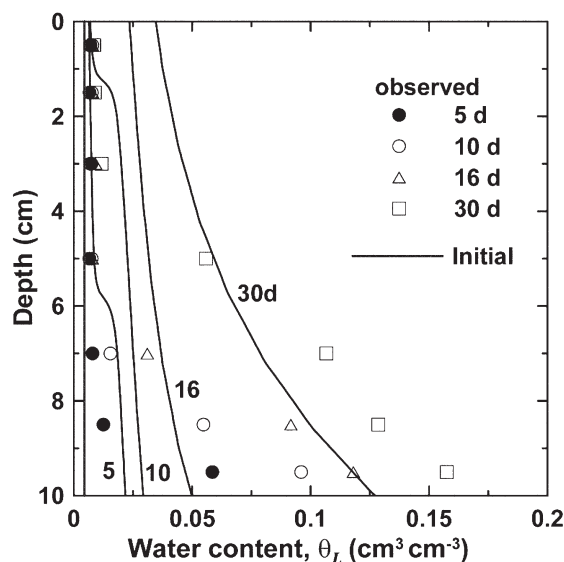

Fig. 3. Comparison of observed water content profiles with those calculated assuming a pore-connectivity coefficient l of 0.5 and an a parameter in the enhancement factor of 8.
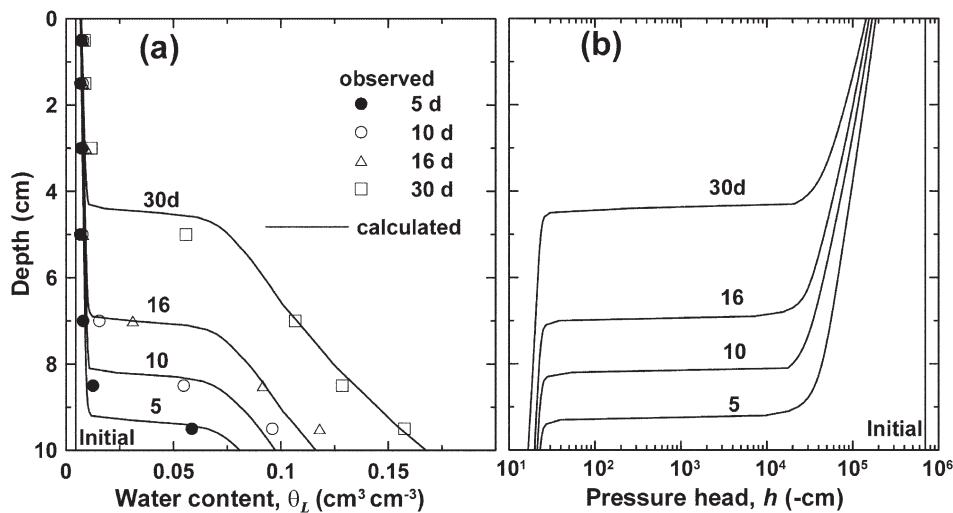
Fig. 4. (a) Comparison of observed water content profiles with those calculated assuming a pore-connectivity coefficient l of 6.17 and an a parameter in the enhancement factor of 8; and (b) simulated pressure head profiles.

relation between the pressure head, h, and the unsaturated hydraulic conductivity, K_{Lh}, is shown in Fig. 1b. Higher values of l lead to a faster decrease in K_{Lh} with decreasing h. Figure 4a shows water content profiles calculated with an optimized value of $l = 6.17$ (for $a = 8$). In this case, the calculated water contents agreed very well with the observed water contents. Figure 4b shows the corresponding pressure head profiles. While pressure heads increased significantly from the initial value ($h = -7 \times 10^5$ cm) in the lower part of the soil column ($-30 \le h \le -20$ cm), the condensation process caused them to remain very low ($-1 \times 10^5 \le h \le -3 \times 10^4$ cm) in the upper part.

Since similar results were obtained with the other two combinations of parameters a and l, these two parameters were mutually correlated and could not be estimated simultaneously from available data, i.e., water content profiles only. For a given experimental setup, only one of these two parameters can be optimized, while the other parameter has to be estimated independently and fixed during calibration. Notice, however, that differences between the optimized hydraulic conductivity functions for different enhancement factors were relatively small and probably below the precision of the available measurement techniques for low water contents, for which hydraulic conductivity measurements are extremely difficult to do.

The agreement between the measured and calculated water contents indicates that the relation of K_{Lh} and h in the Hamaoka dune sand at lower water contents can be described well using Mualem's (1976) pore-size distribution model with the Fayer water retention curve model. The $K_{Lh}(h)$ function shows different gradients, dlogK_{Lh}/dlog$h$, for higher and lower pressure heads. This shape for the $K_{Lh}(h)$ function is similar to that proposed by Tuller and Or (2001), which considers film flow for lower water contents as well as pore water flow for higher water contents. While the sand retains water in soil pores by capillary forces at higher water contents, at lower water contents water is retained on soil particles as water films. These different retention mechanisms may alter the dependency of the hydraulic conductivity on the pressure head. A similar argument was used for solute mixing in terms of the hydrodynamic dispersion in the dune sand (Toride et al., 2003). Solutes mix well in larger pores with higher pore-water velocities and higher water contents. On the contrary, slow solute mixing, primarily by transverse diffusion, becomes dominant for lower water contents.

Figure 5 shows the unsaturated hydraulic conductivity functions, $K_{Lh}(h)$, calculated using the van Genuchten–Mualem (VG) model (van Genuchten, 1980) with various values of l ($-1 \le l \le 5$). Although the VG model shows different values of dlogK_{Lh}/dlog$h$ for different values of l, it never resembles the shape of the Fayer model, which has different values of dlogK_{Lh}/dlog$h$ for different ranges of pressure heads.

the bottom of the soil column. For example, while the calculated θ_L was 0.03, the observed value was 0.096 at a depth of 9.5 cm after 10 d. On the other hand, calculated water contents were overestimated in the middle of the column (e.g., calculated $\theta_L = 0.025$ vs. observed $\theta_L = 0.0075$ at a depth of 5 cm after 10 d). This disagreement between observations and calculations might be the result of either overestimation of the upward liquid water flow or underestimation of the downward vapor flow.

Since our focus was mainly on the uncertainty in the unsaturated hydraulic conductivity, K_{Lh}, for lower water contents, we fixed the water vapor flow parameters (i.e., $a = 5$, 8, and 15 in the enhancement factor) and attempted to decrease the upward liquid water flow by adjusting K_{Lh} through changing the pore-connectivity coefficient, l. Optimized values of l using the inverse analysis of the observed water contents were 6.00, 6.17, and 4.91 for $a = 5$, 8, and 15, respectively. The
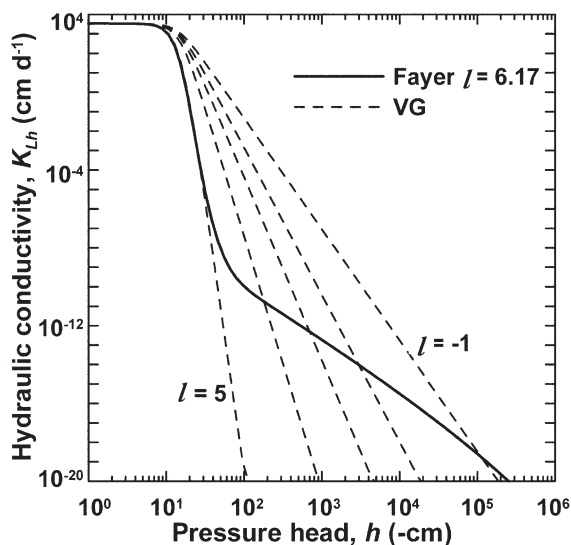

Fig. 5. Relations between the unsaturated hydraulic conductivity and the pressure head described using the van Genuchten–Mualem model (VG), $K_{Lh} = K_s S_e^l [1 - (1 - S_e^{1/m})^m]^2$, for various values of the pore-connectivity factor l (K_s is the saturated hydraulic conductivity, S_e is the effective liquid saturation, and m is an empirical shape parameter), and the Fayer model with l equal to 6.17.

This indicates that the Fayer model not only modifies the VG model for the soil water retention curve, but it also has a profound effect on the unsaturated hydraulic conductivity function for lower water contents.

Since the numerical model that uses the unsaturated hydraulic conductivity function $K_{Lh}(h)$ with the pore connectivity parameter $l = 6.17$ that was optimized for the enhancement factor with $a = 8$ (Fig. 1b and 5) describes the experimental data (Fig. 4) well, the following discussion will be based on calculations with this unsaturated hydraulic conductivity function. It needs to be emphasized here, however, that the optimized unsaturated hydraulic conductivity function may not be unique and could not be independently validated against directly measured hydraulic conductivities at low water contents.

Temperature Profiles

Figure 6 presents the simulated and observed temperature profiles obtained during the experiment. A linear decrease in temperature between the upper and lower boundary values was reached after only 0.1 d. Observed temperatures after 6 and 16 d closely followed this linear distribution, except for small convex deviations at a depth of 9 cm after 6 d and 7 cm after 16 d. This small deviation from the linear profile can be explained by the difference in thermal conductivities between the lower and upper part of the column as a result of their different water contents. For example, the convex deviation occurred at a depth of 7 cm after 16 d, which agreed well with the depth of the moisture front (Fig. 4a). The thermal conductivity calculated using Eq. [14] for the lower part of the column ($\theta_L > 0.075$) was >1.4 W m^{-1} K^{-1}, while it was <0.7 W m^{-1} K^{-1} for the upper part of the column ($\theta_L < 0.01$).

Liquid Water and Water Vapor Fluxes

Once the pressure head and temperature profiles were obtained, it was possible to evaluate the liquid and vapor fluxes due to pressure head (isothermal) and temperature (thermal) gradients using Eq. [1]. Figure 7 shows the calculated total water flux profiles, as well as their four components, after 6 and 16 d. Positive values represent upward movements, while negative values represent downward movements.

The total water flux, q_{Total}, was always directed downward (negative) throughout the column from the warm end to the cold end, similarly as in previous studies of nonisothermal flow in column experiments (Jones and Kohnke, 1952; Nassar et al., 1992a). While the total water flux, q_{Total}, was large in the upper part of the soil column above the moisture front (−0.017 cm d^{-1} after 6 d and −0.02 cm d^{-1} after 16 d), it was much smaller in the lower part of the column with higher water contents (Fig. 4a), and it was zero at the bottom of the column. The downward water movement occurred mainly as thermal water va-
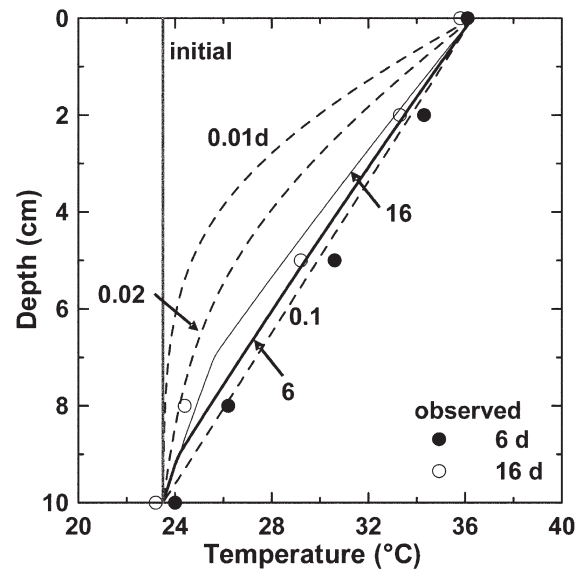
Fig. 6. Comparison of observed and calculated soil temperature profiles.

por flux, q_{vT}, due to the large downward temperature gradient (Fig. 6). The isothermal vapor flux, q_{vh}, was small except near the moisture front (in the 9-cm depth after 6 d and the 7-cm depth after 16 d), where upward vapor flux was calculated due to the large positive pressure head gradient (Fig. 4b). Since q_{vh} was much smaller than q_{vT}, the actual vapor flux, q_v, was downward after both 6 and 16 d.

Upward water movement occurred mainly as isothermal liquid water flux, q_{Lh}, due to the upward pressure head gradient, which developed at the bottom of the soil column as a result of vapor condensation. The isothermal liquid water flux had a peak at both times near the moisture front due to the extremely large pressure head gradients. The isothermal liquid water flux was also large at the bottom of the column after 16 d (0.067 cm d^{-1}) because of the large unsaturated hydraulic conductivity, K_{Lh}, for high water contents. As the water content gradually increased at the column bottom and the moisture front moved upward, so did the maxima and absolute values of q_{Lh} and q_{vT}. The thermal liquid water flux, q_{LT}, showed
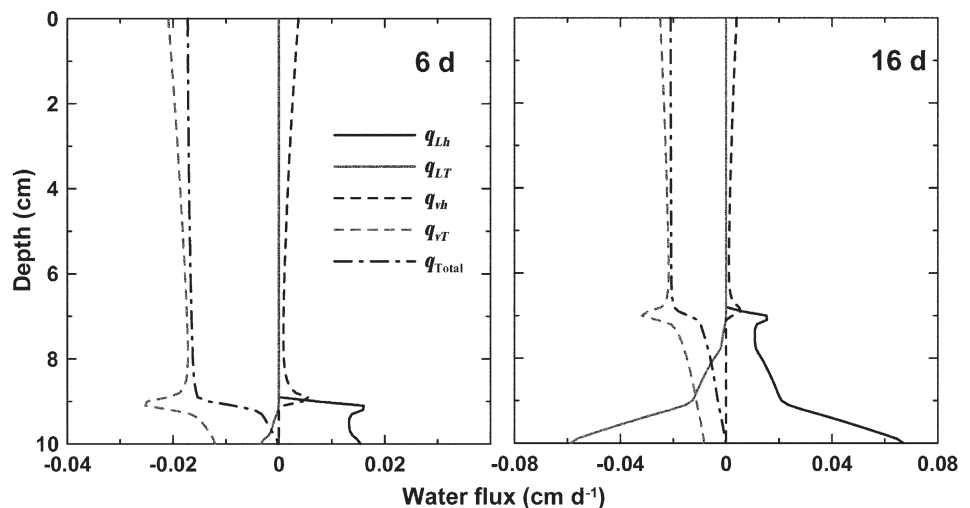
Fig. 7. Calculated profiles of the thermal liquid and vapor (q_{LT} and q_{vT}, respectively) and isothermal liquid and vapor (q_{Lh} and q_{vh}, respectively) fluxes and the total water flux (q_{Total}) at 6 d (left) and 16 d (right) (positive fluxes are directed upward).
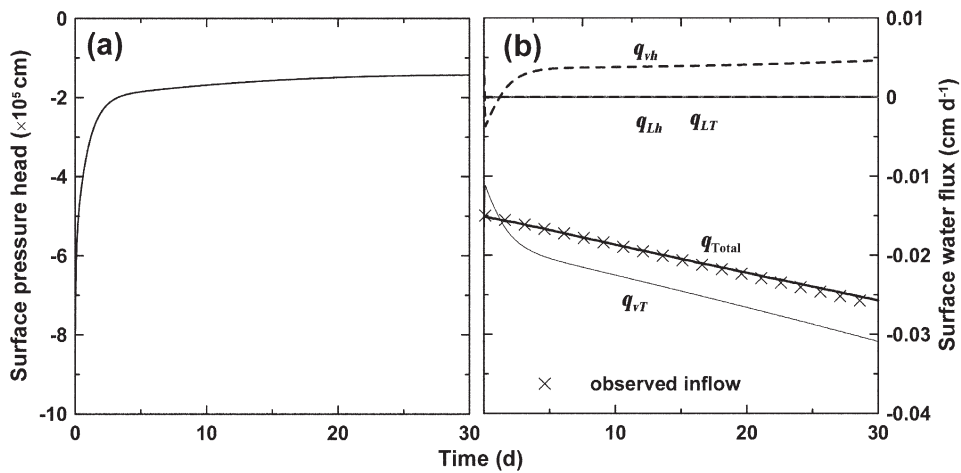
Fig. 8. Calculated (a) surface pressure heads and (b) surface thermal liquid and vapor (q_{LT} and q_{vT}, respectively) and isothermal liquid and vapor (q_{Lh} and q_{vh}, respectively) fluxes and the total water flux (q_{Total}) as a function of time.

downward water movement near the bottom of the column. Although q_{LT} was small after 6 d, it increased after 16 d (-0.06 cm d^{-1} at the bottom) due to a larger thermal hydraulic conductivity, K_{LT} (Eq. [8] with the large K_{Lh}). Because q_{Lh} was larger than q_{LT} at every depth, the actual liquid water flux, q_L, was always upward. The value of q_L was negligibly small at depths above the moisture front after both 6 and 16 d.

Miyazaki (1976) calculated the increase in water contents at the bottom of the columns by evaluating the water vapor flux due to the temperature gradient using the Philip and de Vries theory and the Penman theory (Penman, 1940), which was the original theory of water vapor flow without the enhancement factor. The water content calculations significantly overestimated the observed values, however, because of the difficulty of calculating the simultaneous upward liquid flux resulting from the water content increase. Our numerical simulations of the coupled movement of water vapor, liquid water, and heat could consider simultaneously all four flux components and thus lead to better agreement between simulated and observed water contents.

Surface Boundary Condition

Both Milly (1984) and Saito et al. (2006) evaluated surface water flux. The former used meteorological variables, while the latter utilized the surface energy balance. Since evaluating water movement inside the soil column was the primary purpose of this study, the observed amount of water vapor diffused into the column, $q_{Total}(0,t)$, was determined from weight changes in the entire soil column and used as the surface boundary condition for water flow. We assumed that $q_{Total}(0,t)$ was equal to the sum of liquid and vapor fluxes passing through the surface boundary, as described by Eq. [16]. The four components of the total flux at the soil surface were then determined using the pressure head and temperature gradients, as described by Eq. [1]. Each flux may have a different magnitude and direction depending on the pressure head and temperature gradients at the soil surface. Since the temperature in the soil column quickly established steady-state conditions (during about 0.1 d as shown in Fig. 6), the pressure head at the soil surface was the only other variable that could adjust q_{Total} to be equal to the

observed diffusion flux of water vapor into the column during calculations.

Figure 8a presents the calculated surface pressure heads during the experiment. Although not clearly visible in Fig. 8a, at the beginning of the experiment the surface pressure head first decreased quickly from the initial pressure head of -7×10^5 cm, and then increased because of the rapid change in the surface temperature from the initial value of 23.5°C to the imposed boundary value of 36.3°C. After that, the surface pressure head started increasing steadily until it reached a value of around -1.5×10^5 cm. The increasing pressure head reflects vapor condensation at the soil surface. As the amount of condensed water was relatively small, water content increases were barely noticeable.

Figure 8b shows the four components of the surface flux $q_{Total}(0,t)$ as a function of time. Liquid water fluxes (q_{Lh} and q_{LT}) were significantly smaller (and in fact negligible) than vapor fluxes (q_{vh} and q_{vT}) because the hydraulic conductivities for liquid water were several orders of magnitude smaller ($K_{Lh} \approx 10^{-19}$ cm d^{-1} and $K_{LT} \approx 10^{-15}$ cm^2 K^{-1} d^{-1}) than vapor hydraulic conductivities ($K_{vh} \approx 10^{-6}$ cm d^{-1} and $K_{vT} \approx 10^{-1}$ cm^2 K^{-1} d^{-1}). Although the direction of q_{vh} was changing at the beginning of the experiment, due to oscillations of the surface pressure head in time (Fig. 8a), downward q_{vT} and upward q_{vh} dominated the overall water flux $q_{Total}(0,t)$, and defined the water vapor diffusion into the column.

Condensation and Evaporation Rates

The evaporation rate (E) at each internal discretization node can be calculated with a discretized form of Eq. [3]:

$$E_i^j = -\frac{\theta_{Li}^j - \theta_{Li}^{j-1}}{\Delta t} + \frac{q_{Li-1/2}^{j-1/2} - q_{Li+1/2}^{j-1/2}}{\Delta z} \qquad [19]$$

where the subscript i represents the position of a lattice point and the superscripts j and $j-1$ denote the current and previous time points, respectively.

The evaporation rate at locations $i = 1 + 1/4$ and $i = N - 1/4$ can be evaluated using a method similar to Eq. [19], where $i = 1$ and N represent the lower and upper boundary nodal points, respectively:

$$E_{1+1/4}^j = -\frac{\theta_{L1+1/4}^j - \theta_{L1+1/4}^{j-1}}{\Delta t} + \frac{q_{L1}^{j-1/2} - q_{L1+1/2}^{j-1/2}}{\Delta z/2} \qquad [20]$$

$$E_{N-1/4}^j = -\frac{\theta_{LN-1/4}^j - \theta_{LN-1/4}^{j-1}}{\Delta t} + \frac{q_{LN}^{j-1/2} - q_{LN-1/2}^{j-1/2}}{\Delta z/2} \qquad [21]$$

Values at $i = 1 + 1/4$ and $i = N - 1/4$ (e.g., $\theta_{L1+1/4}$) can be obtained using a linear interpolation of adjacent node values. Note that q_{L1} does not have to be zero because, as described by Eq. [17], only the total boundary flux is assumed to be zero.

The evaporation rate at the surface boundary, E_1, is evaluated by linearly extrapolating $E_{1+1/4}$ and E_2 toward the surface. A similar linear extrapolation from $E_{N-1/4}$ and E_{N-1} is made to estimate E_N.

Figure 9a displays evaporation rate profiles calculated using Eq. [19–21]. Note that negative evaporation represents vapor condensation. The maximum evaporation rate was located at a depth of 9 cm after 6 d, and moved upward to a depth of 7 cm after 16 d. This localized evaporation resulted in the maximum downward thermal vapor flux, q_{vT}, behind the moisture front as shown in Fig. 7. Figure 9b shows relative humidity profiles (Table 1) at 6 and 16 d. The relative humidity decreased from almost unity near the bottom of the column to 0.98 at the moisture front. The location of the maximum evaporation rate corresponded exactly with the position of the abrupt decrease in the relative humidity. As shown in Fig. 4b, a large pressure head drop occurred at the moisture front ($h = -2 \times 10^4$ cm), resulting in a decrease in the relative humidity.

Vapor condensation started just below the maximum evaporation peak, where the relative humidity increased to almost unity. Vapor had to condensate at this position because the air could not hold all the water vapor coming from the upper location. As shown in Fig. 6, vapor moved farther down and eventually condensed at the cold end. The maximum condensation (minimum evaporation) rate occurred at the bottom of the column: -0.123 d^{-1} after 6 d and -0.085 d^{-1} after 16 d (Fig. 9a).

The total amount of vapor condensation in an entire soil column can be obtained by integrating the condensation rate profile (negative evaporation rate in Fig. 9a) with depth and time. Figure 10 shows the cumulative amount of condensation as a function of time. The total quantity of condensation in the soil profile includes not only the condensation at the bottom, but also that in the rest of the soil profile. The condensation at the bottom dominated initially and accounted for 40% of the total condensation during the first 5 d. Condensation inside the column subsequently increased and reached about 75% of the total condensation (25% at the bottom) after 20 d. The observed cumulative amount of water vapor diffused into the column was also plotted in Fig. 10. Note that the total amount of condensation in the column was greater than the cumulative amount of water vapor diffused into the column due to internal evaporation (Fig. 9a). In other words, the difference between the total amount of condensation and the cumulative amount of diffusion into the column was equal to the amount of evaporation inside the column. The amount of internal evaporation accounted for around 25% of the total condensation, regardless of the time.

Enhancement Factor

The impact of the enhancement factor, η, can also be demonstrated using water content profiles. Figure 11 shows
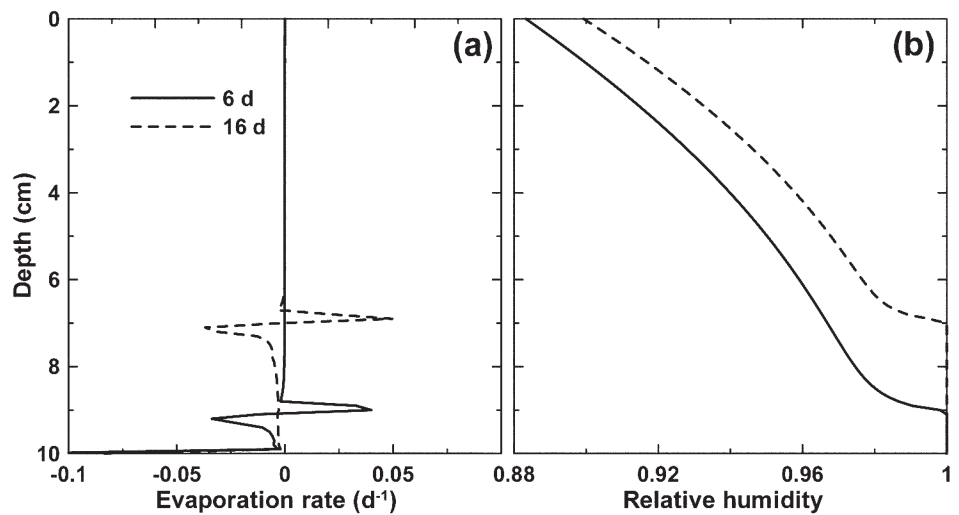

Fig. 9. Calculated profiles of (a) the evaporation rate and (b) the relative humidity.

the observed water content profiles as well as those calculated with different enhancement factors after 30 d with an optimized value of $l = 6.17$. In calculations without the enhancement factor ($\eta = 1$), calculated water contents were underestimated in the lower part of the column and overestimated in the upper part. More vapor condensed in the upper part of the column due to underestimation of the vapor flow. This simulation clearly demonstrates the importance of considering the enhancement factor. Calculated water content profiles were similar when different values of the a coefficient ($a = 5$, 8, and 15) were used to calculate the enhancement factor (Fig. 11). Figures 12a and 12b show profiles of the liquid water and water vapor fluxes and the evaporation rate, calculated with $a = 8$ and 15. Both the downward vapor flux and the upward liquid water flux increased as the enhancement factor increased, and so did both the maximum evaporation and condensation rates. The amount of water circulating in the soil column increased as the enhancement factor increased. These two opposing effects (evaporation and condensation) compensated for each other,
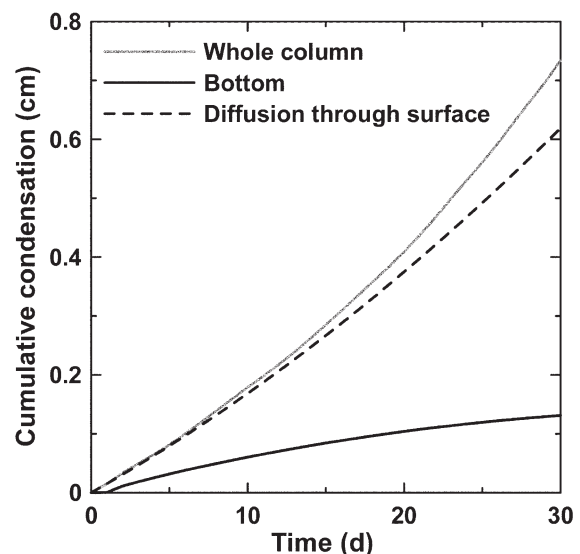

Fig. 10. Cumulative condensation amounts in the whole soil column and at the bottom of the soil column compared with the cumulative amount of water vapor diffused through the surface as a function of time.
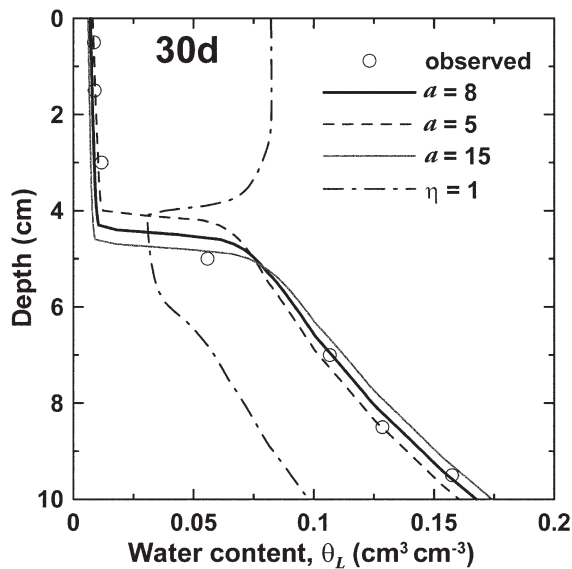
Fig. 11. Water content profiles after 30 d calculated using various values of the enhancement factor (a = 5, 8, 15 and η = 1).

making the impact of the enhancement factor less important for the water content profile in the condensation process.

We have also evaluated the impact of η on the estimation of the pore-connectivity coefficient, l. Optimized l values were 6.00, 6.19, and 4.91 for the enhancement factor a parameters of 5, 8, and 15, respectively. As shown in Fig. 1b, there is only a relatively small range of uncertainty in the unsaturated hydraulic conductivity function due to differences in η for lower pressure heads. As discussed above, however, these two parameters are mutually highly correlated for given experimental data and only one of them can be optimized independently. Additional data need to be measured so that both the pore-connectivity parameter l and the enhancement factor η can be estimated simultaneously.

CONCLUSIONS

We have numerically analyzed the vapor condensation experiments reported by Miyazaki (1976). These experiments involved vapor diffusion and condensation in laboratory sand columns due to an imposed temperature gradient. The movement of water vapor and liquid water in the sand column were evaluated using the Philip and de Vries (1957) model. The coupled transport of water vapor, liquid water, and heat were calculated using the HYDRUS-1D code that included vapor flow.

The numerical model was calibrated against experimental data by optimizing the pore-connectivity coefficient, l, of the unsaturated hydraulic conductivity function for different values of the enhancement factor η. The Fayer and Simmons (1995) model, describing soil hydraulic properties with an estimated l parameter of 6.17 (for the enhancement factor with a = 8), provided a very good agreement between simulated and observed water contents. The rate of decrease in the unsaturated hydraulic conductivity with decreasing pressure head, described by the Fayer model, differed for high and low water contents, reflecting capillary pore water flow and film flow, respectively. It was concluded that the Fayer model with the calibrated l parameter of Mualem's pore-size distribution model worked well for simulating water flow in sandy soils at low water contents. Due to the lack of directly measured unsaturated hydraulic conductivities, however, the calibrated hydraulic conductivity function could not be independently validated. Mutual correlation between the pore-connectivity coefficient and the enhancement factor also raises a question of uniqueness of the optimized unsaturated hydraulic conductivity function.

Additionally, we quantitatively evaluated the four components of the total water flux: liquid and vapor fluxes driven by pressure head and temperature gradients. The evaporation and condensation rates inside the soil column were described further by analyzing these water fluxes. Water vapor that entered the soil column from the hot surface moved downward due to the temperature gradient and condensed at the cold bottom end of the column. Liquid water subsequently moved upward due to the pressure head gradient and evaporated at the moisture front where the relative humidity decreased from 1 to 0.98. Vapor generated by evaporation then moved downward together with vapor coming from the soil surface. A certain amount of vapor condensed just below the location with maximum evaporation at the moisture fronts, and the maximum condensation occurred at the cold bottom of the column (25–40% of the total condensation in the column). Liquid water and water vapor circulated between the bottom of the column and the moisture front, accompanied by condensation and evaporation processes in the sand column.

The impact of the enhancement factor on vapor fluxes inside the soil column was also demonstrated. Downward vapor flux was significantly underestimated when the enhancement factor was neglected. Calculated water content profiles were very similar when the a parameter from the function of the enhancement factor was >5. Higher enhancement factors produced larger upward liquid water
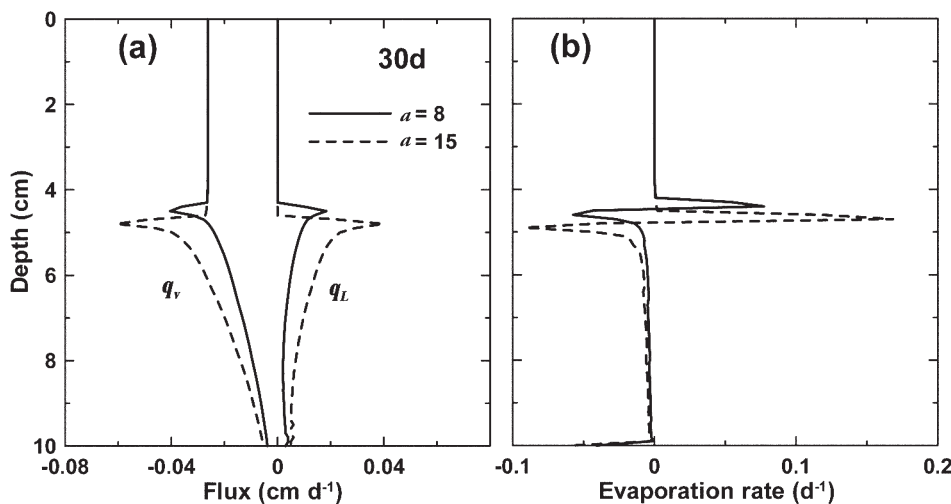

Fig. 12. A comparison of profiles of (a) liquid water and water vapor fluxes (q_L and q_v, respectively) and (b) evaporation rates simulated using a parameter values of 8 and 15 in the enhancement factor.

fluxes and evaporation rates, as well as downward vapor fluxes and condensation rates. These two opposing effects compensated for each other, making the water content profiles in the condensation experiment less sensitive to the enhancement factor. This indicates that water content profiles do not provide enough information to simultaneously estimate both the unsaturated hydraulic conductivity function and the enhancement factor. Additional data are needed so that both the pore-connectivity parameter l and the enhancement factor η can be estimated simultaneously.

ACKNOWLEDGMENTS

REFERENCES

Cahill, A.T., and M.B. Parlange. 1998. On water vapor transport in field soils. Water Resour. Res. 34:731–739.

Campbell, G.S. 1985. Soil physics with BASIC. Elsevier, New York.

Cass, A., G.S. Campbell, and T.L. Jones. 1984. Enhancement of thermal water vapor diffusion in soil. Soil Sci. Soc. Am. J. 48:25–32.

Chung, S.O., and R. Horton. 1987. Soil heat and water flow with a partial surface mulch. Water Resour. Res. 23:2175–2186.

de Vries, D.A. 1958. Simultaneous transfer of heat and moisture in porous media. Trans. Am. Geophys. Union 39:909–916.

Eching, S.O., and J.W. Hopmans. 1993. Optimization of hydraulic functions from transient outflow and soil water pressure data. Soil Sci. Soc. Am. J. 57:1167–1175.

Farlow, S.J. 1993. Partial differential equations for scientists and engineers. Dover, New York.

Fayer, M.H., and C.S. Simmons. 1995. Modified soil water retention functions for all matric suctions. Water Resour. Res. 31:1233–1238.

Fujimaki, H., and M. Inoue. 2003. A transient evaporation method for determining soil hydraulic properties at low pressure. Vadose Zone J. 2:400–408.

Hillel, D. 1971. Soil and water: Physical principles and processes. Academic Press, New York.

Hopmans, J.W., J. Šimůnek, and K.L. Bristow. 2002. Indirect estimation of soil thermal properties and water flux using heat pulse probe measurements: Geometry and dispersion effects. Water Resour. Res. 38(1):1006, doi:10.1029/2000WR000071.

Inoue, M., J. Šimůnek, J.W. Hopmans, and V. Clausnitzer. 1998. In situ estimation of soil hydraulic functions using a multistep soil-water extraction technique. Water Resour. Res. 34:1035–1050.

Jones, H.E., and H. Kohnke. 1952. The influence of soil moisture tension on vapor movement of soil water. Soil Sci. Soc. Am. Proc. 16:245–248.

Klute, A., and C. Dirksen. 1986. Hydraulic conductivity and diffusivity: Laboratory methods. p. 687–734. *In* A. Klute (ed.) Methods of soil analysis. Part 1. Physical and mineralogical methods. 2nd ed. Agron. Monogr. 9. ASA and SSSA, Madison, WI.

Marquardt, D.W. 1963. An algorithm for least-squares estimation of nonlinear parameters. SIAM J. Appl. Math. 11:431–441.

Millington, R.J., and J.M. Quirk. 1961. Permeability of porous solids. Trans. Faraday Soc. 57:1200–1207.

Milly, P.C.D. 1984. A simulation analysis of thermal effects on evaporation. Water Resour. Res. 20:1087–1098.

Miyazaki, T. 1976. Condensation and movement of water vapor in sand under temperature gradient. (In Japanese.) Trans. Jpn. Soc. Irrig. Drain. Rural Eng. 61:1–8.

Monteith, J.L., and M.H. Unworth. 1990. Principles of environmental physics. 2nd ed. Edward Arnold, London.

Mualem, Y. 1976. A new model for predicting the hydraulic conductivity of unsaturated porous media. Water Resour. Res. 12:513–522.

Nassar, I.N., A.M. Globus, and R. Horton. 1992a. Simultaneous soil heat and water transfer. Soil Sci. 154:465–472.

Nassar, I.N., and R. Horton. 1989. Water transport in unsaturated nonisothermal salty soil: II. Theoretical development. Soil Sci. Soc. Am. J. 53:1330–1337.

Nassar, I.N., and R. Horton. 1992. Simultaneous transfer of heat, water, and solute in porous media: I. Theoretical development. Soil Sci. Soc. Am. J. 56:1350–1356.

Nassar, I.N., and R. Horton. 1997. Heat, water, and solute transfer in unsaturated porous media: I. Theory development and transport coefficient evaluation. Transp. Porous Media 27:17–38.

Nassar, I.N., R. Horton, and A.M. Globus. 1992b. Simultaneous transfer of heat, water, and solute in porous media: II. Experiment and analysis. Soil Sci. Soc. Am. J. 56:1357–1365.

Nimmo, R.J. 1990. Experimental testing of transient unsaturated flow theory at low water content in a centrifugal field. Water Resour. Res. 26:1951–1960.

Nimmo, J.R., and E.E. Miller. 1986. The temperature dependence of isothermal moisture vs. potential characteristics of soils. Soil Sci. Soc. Am. J. 50:1105–1113.

Noborio, K., K.J. McInnes, and J.L. Heilman. 1996. Two-dimensional model for water, heat, and solute transport in furrow-irrigated soil: I. Theory. Soil Sci. Soc. Am. J. 60:1001–1009.

Penman, H.L. 1940. Gas and vapor movement in soil: I. The diffusion of vapors in porous solids. J. Agric. Sci. 30:437–462.

Philip, J.R., and D.A. de Vries. 1957. Moisture movement in porous materials under temperature gradients. Trans. Am. Geophys. Union 38:222–232.

Romano, N., and A. Santini. 1999. Determining soil hydraulic functions from evaporation experiments by a parameter estimation approach: Experimental verifications and numerical studies. Water Resour. Res. 35:3343–3359.

Rossi, C., and J.R. Nimmo. 1994. Modeling of soil water retention from saturation to oven dryness. Water Resour. Res. 30:701–708.

Saito, H., J. Šimůnek, and B.P. Mohanty. 2006. Numerical analysis of coupled water, vapor, and heat transport in the vadose zone. Vadose Zone J. 5:784–800.

Scanlon, B., K. Keese, R.C. Reedy, J. Šimůnek, and B.J. Andraski. 2003. Variations in flow and transport in thick desert vadose zones in response to paleoclimatic forcing (0–90 kyr): Field measurements, modeling, and uncertainties. Water Resour. Res. 39(7):1179, doi:10.1029/2002WR001604.

Schaap, M.G., F.J. Leij, and M.Th. van Genuchten. 2001. ROSETTA: A computer program for estimating soil hydraulic parameters with hierarchical pedotransfer functions. J. Hydrol. 251:163–176.

Šimůnek, J., M. Šejna, H. Saito, M. Sakai, and M.Th. van Genuchten. 2008a. The HYDRUS-1D software package for simulating the movement of water, heat, and multiple solutes in variably saturated media. Version 4.0. HYDRUS Softw. Ser. 3. Dep. of Environ. Sci., Univ. of California, Riverside.

Šimůnek, J., M.Th. van Genuchten, and M. Šejna. 2008b. Development and applications of the HYDRUS and STANMOD software packages, and related codes. Vadose Zone J. 7:587–600.

Šimůnek, J., O. Wendroth, and M.Th. van Genuchten. 1998. Parameter estimation analysis of the evaporation method for determining soil hydraulic properties. Soil Sci. Soc. Am. J. 62:894–905.

Toride, N., M. Inoue, and F.J. Leij. 2003. Hydrodynamic dispersion in an unsaturated dune sand. Soil Sci. Soc. Am. J. 67:703–712.

Tuller, M., and D. Or. 2001. Hydraulic conductivity of variably saturated porous media. Film and corner flow in angular pore space. Water Resour. Res. 37:1257–1276.

van Genuchten, M.Th. 1980. A closed-form equation for predicting hydraulic conductivity of unsaturated soils. Soil Sci. Soc. Am. J. 44:892–898.